ARTICLE

Received 00th January 20xx,

Accepted 00th January 20xx

DOI: 10.1039/x0xx00000x

A Liquid-Crystalline Non-Fullerene Acceptor Enabling High-Performance Organic Solar Cells

Pierluigi Mondelli,[a,c] Francesco Silvestri,[b] Laura Ciammaruchi,[b] Eduardo Solano,[d] Eduardo Beltrán-Gracia,[c] Esther Barrena,[b] Moritz Riede[a] and Graham Morse*[c]

The use of liquid crystalline (LC) compounds in organic photovoltaics has revealed to be an effective strategy to optimise the bulk heterojunction morphology, repairing structural defects through their self-assembling properties. Nonetheless, the design of LC materials has mostly been limited to donor molecules in previous reports. Here we introduce a Non-Fullerene Acceptor (NFA), 4TICO, characterised by an improved structural flexibility, which is imparted by the alkoxy sidechain and favours the formation of LC phases at high temperature. This structural polymorphism also occurs in films where the 4TICO is blended with the PBTZT-stat-BDTT-8 polymer. The high-temperature LC polymorph brings to the formation of a smooth surface morphology with less structural defects, providing solar cells with improved short-circuit current (Jsc) and fill factor (FF), by 14% and 20% respectively. An in-depth investigation of the NFA structural properties in relation to the solar cells performance and charge transport is carried out in comparison to the 4TIC crystalline isomer.

Introduction

Organic Photovoltaics (OPV) has become an established research topic in alternative renewable energies, offering a sustainable solution with unique advantages in comparison to conventional silicon photovoltaic technologies.[1] The main benefits of OPV modules result from their low cost and environmental footprint, along with desirable form factor being lightweight, flexible and semi-transparent.[2]

In recent years a growing interest in solution-processed OPVs has been driven by the surge in the performance, now yielding to Power Conversion Efficiencies (PCE) as high as 18% for NFA OPVs.[3] This tremendous progress is a result of progressive optical gap narrowing and energetic alignment at the donor/acceptor interface,[4, 5] along with optimization of the active layer morphology and microstructure.[6-13]

The optimal active layer morphology, often referred to as the bulk heterojunction (BHJ) morphology, is an intermixed blend of an electron donor and acceptor material which ideally phase separates at the nanometre length scale to form a network of pathways (1) to maximise donor-acceptor interface for optimal charge generation and (2) to segregate into pure donor and acceptor phases, ensuring an efficient charge collection at the electrodes and minimizing recombination of opposite charges. Thus, understanding how to control the blend morphology formation is a large body of research in the OPV community and can be achieved by molecular design,[7, 14-19] formulation design,[20-25] and process design.[26-33]

One of the hallmarks of a high performing material (also often essential to its identification) is the ease in which it forms a near ideal BHJ with a simple and reproducible fabrication process. There are many examples of high-performing materials at the time of their discovery such as P3HT, PCBM, PBDB-T and ITIC.[34-36] A common feature among them is our ability to control the BHJ microstructure through post-process annealing at temperatures between 100-150°C which are necessary for the curing of adhesives for lamination in the module production process (while being tolerable from plastic substrates).[37] The chemical design can play an important role to control the material thermal properties, such as glass transition temperature or melting points, in order to match the annealing temperature at which a material can readily diffuse to adjust domain sizes and purity (avoiding excessive phase separation).

Some OPV materials have been found to have liquid crystalline (LC) properties, giving them a wider range of thermal transitions with self-assembling properties and healing effect on grain boundaries and defects.[38, 39] To the best of our knowledge, the fabrication of organic solar cells with liquid crystalline materials in the active layers has been mostly limited to donor molecules, such as hexabenzocorene (HBC),[40-45] phthalocyanine (Pc),[46, 47] porphyrin[48] and triphenylene (TP),[49, 50] but also more recently

[a] Clarendon Laboratory, University of Oxford, Parks Road, Oxford, OX1 3PU, United Kingdom.
[b] Institut de Ciència de Materials de Barcelona, ICMAB-CSIC, Campus UAB, 08193 Bellaterra, Spain.
[c] Merck Chemicals Ltd, Chilworth Technical Centre, University Parkway, Southampton, SO16 7QD, United Kingdom. Email: graham.morse@gmail.com
[d] ALBA Synchrotron Light Source, NCD-SWEET beamline, Cerdanyola del Vallès, 08290 Spain.

† Footnotes relating to the title and/or authors should appear here.
Electronic Supplementary Information (ESI) available: [details of any supplementary information available should be included here]. See DOI: 10.1039/x0xx00000x

developed compounds such as naphtodithiophene[51] and BTR derivatives[52-55]. A rare example of liquid crystalline acceptors do exist such as fullerene-containing hexaalkoxyloxytriphenylenes compounds with columnar mesophases.[56] For most of the cases, active layers including a liquid crystalline donor has demonstrated high FF and J_{sc}, which has been attributed to an improved charge transport due to the reduction of recombination centres and a better microstructural ordering.[51, 52, 54]

In this work, we compare two NFA molecules, 4TICO[57] and 4TIC,[58] with a common design of a fused-ring thiophene-thieno[3,2-b]thiophene-thiophene (4T) as the central donor unit and an electron-deficient 3-(dicyanomethylidene)indan-1-one (IC) as the terminal acceptor unit in OPV devices. During our investigation, we identify unique liquid crystalline properties in 4TICO, likely arising from the added structural flexibility and rotational freedom around the oxygen bond in its alkoxy-phenyl sidechain.[59] We highlight how NFA crystallization tendencies can be tuned by sidechain engineering: (1) preventing the drastic phase separation observed at high temperatures in 4TIC films and other similar NFA derivatives[36, 60] and (2) leading to liquid crystal phase behaviour which can be responsible for a severe reduction of the bimolecular recombination and improved power conversion efficiency for PBTZT-stat-BDTT-8:4TICO[61] blends.

Experimental

General Characterization

UV-Vis absorption spectra were recorded on an OceanOptics QE PRO spectrometer using a tungsten halogen light source (HL-2000-FHSA from OceanOptics). The DSC experiment was carried out on a powder sample using a Q1000 model from TA Instruments at a heating rate of 20°C min^{-1} and under a constant nitrogen flux of 50 ml min^{-1}. Polarised optical microscopy (POM) studies were carried out by using Olympus BH-2 microscope equipped with two polarisers that were operated crossed with the sample in between. A Metler Toledo FP82HT hot stage with a Metler Toledo FP90 controller and an Infinity 2 camera. Powder X-ray diffraction was performed using a PANalytical X'Pert PRO diffractometer with Cu -Kα radiation. Preliminary Raman scattering measurements in the 200-4000 cm^{-1} range were also performed. However, with the obtained spectral response it was not possible to pursue the NFA polymorphism at different temperatures like in other techniques presented throughout the work.

Grazing Incidence Wide Angle X-Ray Scattering (GIWAXS)

The GIWAXS experiments were carried out at NCD-SWEET beamline at ALBA synchrotron (Beamtime ID: 2019093873). A monochromatic X-ray beam with a photon energy of 12.4 keV was set using a Si (1 1 1) channel cut monochromator, further collimated with an array of beryllium lenses. The 2D GIWAXS maps were recorded with a Rayonix LX 255-HS detector, consisting of a pixel array of 960 × 2880 pixels of 88.54 × 88.54 μm^2 (H × V) for the binning employed. The samples were thermally annealed using an adapted Linkam TMSH 600 stage for grazing incidence experiments that maintains the sample under a continuous room temperature N_2 flow. The *in situ* thermal experiments were performed at 100°C, 120°C, 140°C and 180°C with a thermal ramp of 50°C/min and then actively cooled down (at the same rate) to room temperature using a liquid N_2 flow. At each annealing step, after keeping the sample at the selected temperature for 5 min, 2D GIWAXS frames were acquired near the critical angle of the substrate (ca. 0.15°), being surface sensitive and minimizing the contribution of the substrate. The recorded 2D scattering patterns were analysed using a home-made python routine based on pyFAI (the Fast Azimuthal Integration Python library).[62] 2D GIWAXS images are in logarithmic scale, ranging from dark blue (low intensity) to yellow (high intensity).

It has to be noted that the *in situ* annealing protocol slightly differs from the one employed for the device optimization using a hot plate (see below). Nevertheless, *ex situ* GIWAXS analysis on the devices has confirmed the same structural evolution with annealing although with small shifts in the temperature attributed to the different thermal history in the two cases.

Atomic Force Microscopy

The films were systematically investigated by AFM both in contact and dynamic modes using a commercial head and control unit from Nanotec Electronica. The used thermal annealing protocol was the one optimized for the devices (see below). For each sample, after each annealing step, different spots of the surface were imaged (at several image sizes) to have a statistical validity of the measurements. The images presented in the article are chosen as high-resolution representative images of the surface. The estimation of the root mean square (RMS) roughness was done selecting about 6 contact mode images (30x30 and 50x50 μm^2) for each temperature. Si_3N_4 V-shaped cantilevers (Veeco) with the nominal force constant ranging between 0.03 and 0.5 N/m were employed for the contact mode, while Cr/Pt-coated silicon tips on rectangular cantilevers (BudgetSensors) with a nominal resonance frequency of 75 kHz and a force constant of 3 N/m were used for the dynamic mode. The WSxM freeware was used to analyse all the presented AFM images.[63]

Solar Cells Fabrication and Characterization

Inverted-architecture organic solar cells were fabricated by blade coating of the organic layers on Indium Tin Oxide(ITO)/glass pre-patterned 5x5 cm^2 substrates. A 30 nm thick layer of Aluminium-doped Zinc oxide from Avantama (N-21X-Slot) was cast as received, using a 50 µm blade gap, 40 µL cast volume, 4 mm s^{-1} blade speed on a 40 °C casting plate. The layer was then annealed on a hotplate at 100°C for 10 minutes in air. PBTZT-stat-BDTT-8:4TIC/4TICO active layers were processed from o-Xylene solutions at 23 mg ml^{-1} in 1:1.3 ratio

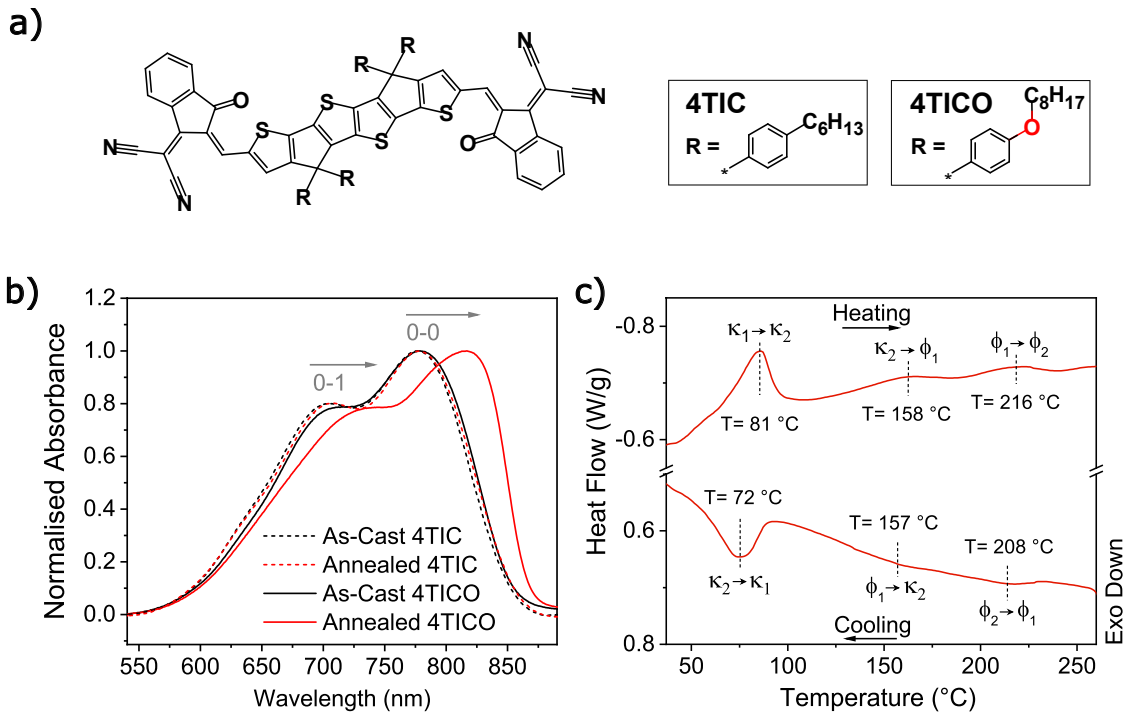

Figure 1 a) 4TIC and 4TICO chemical structures. (b) UV-vis absorption spectra acquired on the as-cast and 140°C annealed films. 4TICO main vibronic peaks (0-0 and 0-1) redshifts upon annealing are highlighted. c) Multiple 4TICO enantiotropic transitions are visible in the Differential Scanning Calorimetry thermogram.

(by weight) without the use of any additional additive, using a 100 µm blade gap, 70 µL cast volume on a 60 °C casting plate. The blade speed was adjusted between 7 to 13 mm s^{-1} to reach the desired thickness of 80 nm. A 50 nm thick layer of PEDOT:PSS (Clevios Al 4083 from Heraeus) was used as a Hole Transporting Layer (HTL), using a blade gap of 575 µm, 180 µL cast volume, 20 mm s^{-1} blade speed on a 65 °C casting plate. Finally, a 100 nm silver back electrode was thermally evaporated on top of the HTL, under a pressure of 2×10^{-6} mbar at a rate of 1 Å/s. The current-voltage characteristics were measured in an inert nitrogen glove box system, using a AM1.5G solar simulator at 1Sun intensity (Oriel Sol1A, 94041A from Newport), as calibrated with a KG5 filtered Si-photodiode (Newport 91150V). All the samples were measured before and after each annealing step (five minutes at 100°C, five minutes at 120°C, three minutes at 140°C) followed by a two-minute cooling step by placing the samples on a cold (room temperature) metallic surface.

Photo-CELIV

Photo-CELIV allows to simultaneously study the charge carrier mobility and recombination[64-71] of solar cells with optimised thicknesses and configurations for real-life working conditions[72]. Experiments were carried out by using the photo-CELIV module of the Transient Measurement Unit by Automatic Research. To limit any charge carrier density injection due to non-blocking contacts, the sample was kept at a constant pre-bias voltage (close to V_{oc}) before the application of the linear increasing voltage. The fastest species mobility is determined by the maximum of the current transient.[73] A correct estimation of the mobility was obtained from long time delays (10 µs), following the approach published by Baumann et al.[65] to minimise the superposition of the RC time with the extraction peak (Figure S14).[74, 75] Charge carrier recombination was also studied by varying the time delay between the 655 nm laser pulse and the linearly increasing voltage.[72]

Results and Discussion

4TICO and 4TIC have quite similar chemical structures, see Figure 1a, but we found they exhibit quite different physical properties.

NFAs Thermotropic Properties

Given the identical molecular backbones, 4TIC and 4TICO possess very similar absorption features in the as-cast films (Figure 1b). Nevertheless, the two materials showed different thermotropic behaviours: the 4TICO main absorption peak (the 0-0 vibronic transition) is strongly affected by temperature annealing (absorption maximum redshifts by ~30 nm), while for 4TIC no change is observed in the same temperature range (100-140°C). This spectral change can be attributed to an evolution of the populations characterized by differences in intra-molecular (e.g., conformations) and intermolecular interactions (e.g. packing), suggesting a variation in the 4TICO molecular arrangement.[26] No substantial change was observed for the 4TIC absorption spectra before and after the thermal treatment.

To get a deeper insight into the phase behaviour of 4TICO, we performed differential scanning calorimetry (DSC), polarized optical microscopy (POM) and powder X-Ray Diffraction (XRD).

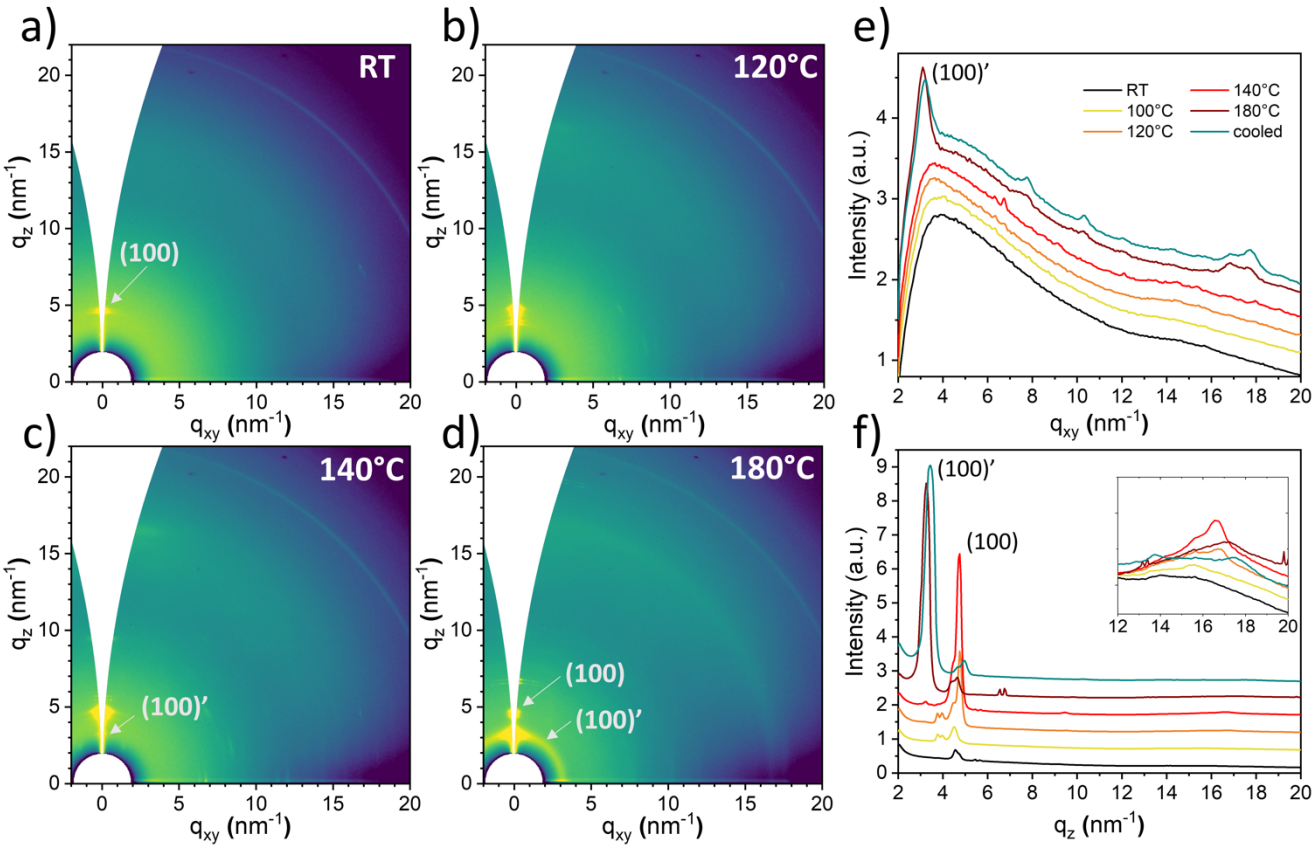

Figure 2 Structural evolution of 4TICO film upon annealing treatment. 2D GIWAXS maps at (a) RT, (b) 120°C, (c) 140°C and (d) 180°C and corresponding (e) IP and (f) OOP profiles. The relevant diffraction features are labelled in the maps.

DSC revealed three enantiotropic transitions within the explored temperature window of 40 to 260 °C (Figure 1c). At room temperature, 4TICO exhibits a crystalline phase as multiple sharp reflections are visible in the powder XRD pattern (Figure S1a). The sharper peak observed at the first analysed temperature (~81°C) during the heating process indicates the formation of a second crystalline (κ_2) phase, as birefringence with no fluidity was observed by POM upon shearing stress (Figure S1b). The two high temperature transitions (observed at 158°C and 216°C) are characterised by lower enthalpies and broader peaks, suggesting the formation of fluid phases (ϕ_1 and ϕ_2) as confirmed by POM images (Figure 1c) and microstructure/morphology analysis presented throughout the text. Cross-polarized POM images (Figure S1c) highlighted the formation of aligned domains upon shearing stress at high temperature. The latter feature is commonly observed in liquid crystal (LC) phases where molecules exhibit orientational order and lack positional order.[76]

NFA microstructure and morphology

For a more in depth understanding of the thin film solid-state arrangement and morphology and to keep track of the structural transformations induced by temperature, we performed *in situ* 2D grazing incidence wide angle x-ray scattering (GIWAXS) and atomic force microscopy (AFM) at different annealing temperatures.

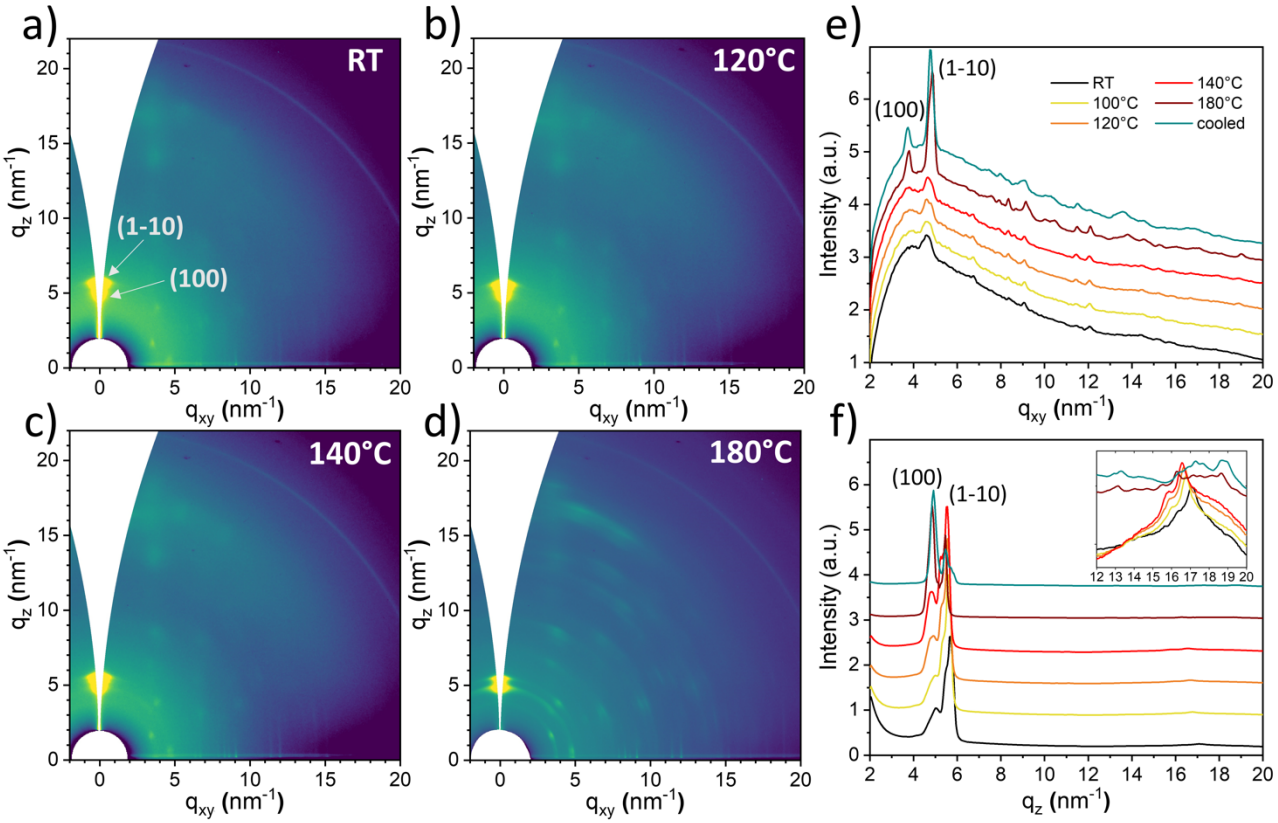

Figure 3 Structural evolution of 4TIC film upon annealing treatment. 2D GIWAXS maps at (a) RT, (b) 120°C, (c) 140°C and (d) 180°C and corresponding (e) IP and (f) OOP profiles. The relevant diffraction features are labelled in the maps.

The structural evolution with temperature of the two pure NFAs was monitored by collecting 2D GIWAXS maps during *in situ* experiment in the range from 25 to 180 C°. Figure 2a-d displays the 2D GIWAXS maps of 4TICO for four selected annealing temperatures (additional maps are provided in Figure S2 together with 1D integration profiles). The corresponding in-plane (IP) and out-of-plane (OOP) profiles are also reported (Figure 2e, f). The GIWAXS data indicate that the 4TICO microstructure undergoes significant changes upon annealing, with the competition of two polymorphs in the explored temperature range. At room temperature (RT) one main feature is identified at $q_z \approx 4.6$ nm^{-1} along the OOP direction, which can be generically attributed to the (100) reflection,[77] resulting in a lamellar stacking distance of about 14 Å. Upon annealing, the (100) peak increases in intensity reaching its maximum at 140°C, indicating an enhanced crystallinity (see Figure 2f). Beyond this temperature, a strong decrease of the intensity takes place with a concomitant increase of the full width half maximum (FWHM) of the peak (Figure S2), that according to the Scherrer analysis (Section 2 of Supporting Information) indicates a reduced crystalline order. A new diffraction feature emerges at $q_z \approx 3.2$ nm^{-1} along the OOP, corresponding to a spacing of about 20 Å, being clearly visible after the annealing step at 180°C (Figure 2d). We ascribe the new peak to a larger lamellar stacking associated to a high-temperature liquid-crystalline polymorph (LC phase), labelled as (100)'. At 140 °C, multiple new features rise in the q-region between 15 nm^{-1} and 17 nm^{-1} along the OOP direction (Figure 2b). The associated spacing range (3.5-4 Å) can be attributed to a superposition of the π-π stacking of aromatic units [77, 78] and the liquid-like conformation of molten aliphatic chains.[79] We note that the development at higher temperature of scattering rings with a relative large azimuthal dispersion agrees with the formation of the 4TICO LC phase evidenced by DSC and with the pronounced UV-Vis red-shift and the sample fluidity (with slight differences in the transition temperature due to the different annealing protocol, see Experimental Section). Because of the fast cooling of the film to RT, the structure remains unvaried and 4TICO is quenched into the LC phase.

4TIC is generally more crystalline than 4TICO already at RT, with a richer and more complex diffraction pattern. The GIWAXS 2D maps of 4TIC with the corresponding IP and OOP profiles are shown in Figure 3 (the maps completing the set and the 1D integration profiles can be found in Figure S3). Two main Bragg peaks dominate the diffraction intensity maps at all temperatures, visible along the OOP direction at $q \approx 5.0$ nm^{-1} and $q \approx 5.7$ nm^{-1}. Referring to the structure reported for the 4TIC,[58] we label the two peaks as (100) and (1-10), respectively, implying the coexistence of two preferential orientations. Whereas annealing up to 140°C does not lead to significant

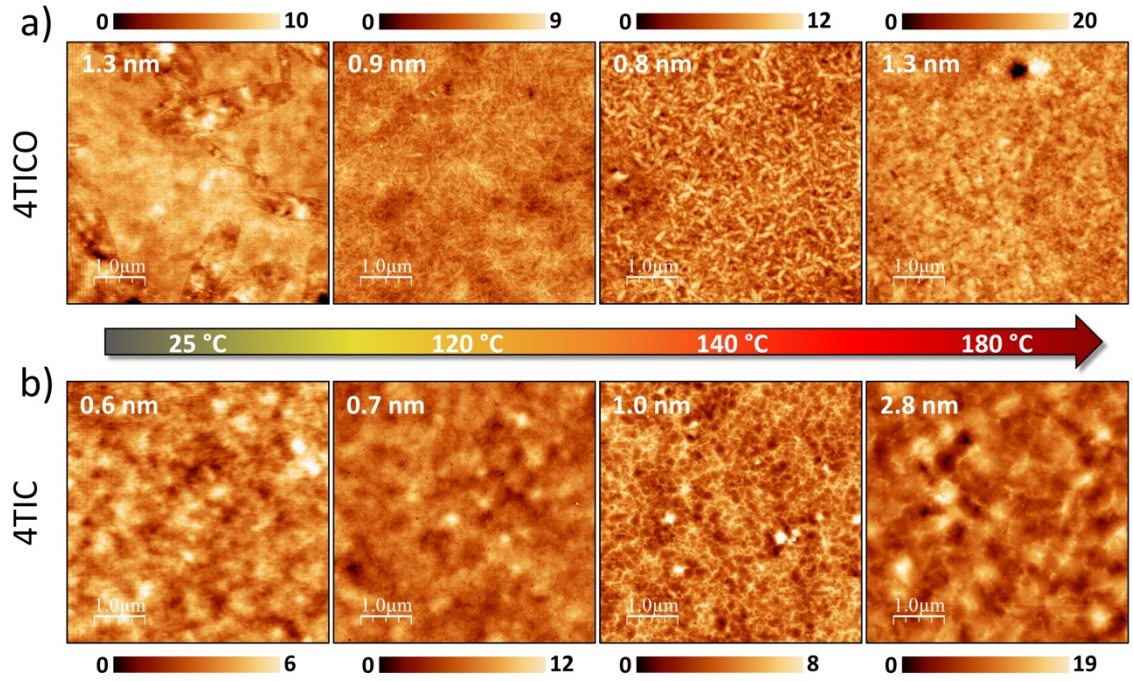

Figure 4. Morphological evolution of (a) 4TICO and (b) 4TIC films (50 nm thick) upon annealing: 5x5 µm² AFM topography images. The values reported in the images represent the RMS roughness and the reported colour scale bars are in nanometres.

changes in the GIWAXS diffraction features of the 2D map, the diffraction pattern becomes clearly sharper upon annealing at 180°C, indicating an overall increased crystallization of 4TIC. It is also observed that annealing at 180°C favours the ordering along the (100) direction, with an increase of intensity and a reduction of FWHM of the (100) peak (Figure S3). As for 4TICO, also in the case of 4TIC the structure remains after cooling the sample down to RT although with a slight decrease of the diffraction signal intensity.

In summary, 4TICO undergoes a transition between two polymorphs upon thermal annealing (140°C<T<180°C), where the LC phase emerges with a larger orientation distribution and lower mean domain size as compared to the crystalline phase formed at lower temperatures. In contrast, 4TIC exhibits a higher degree of crystallinity at RT, which is significantly enhanced upon thermal annealing for T>140°C, indicating crystallization of the NFA. It is evident that the longer and bulkier sidechains in 4TICO act as a steric hindrance for the molecular crystallization leading to a different phase behaviour.

The structural changes also manifest themselves in the morphology of the films. Figure 4 shows representative topographical images measured by AFM (contact mode) for the two NFA films at different annealing steps (images at a different scale are reported in Figure S4). The pristine non-annealed 4TICO film appears homogeneous with sharp-edged sheet-like features. The topography changes upon annealing at T>120°C at which short filamentary features start to be distinguished to further dominate the morphology upon annealing beyond 140°C. The length and thickness of these needle-like elements are estimated by profile analysis to be up to 500 nm and 150 nm, respectively. In spite of the morphological changes, the surface roughness remains in the same range (Figure S4). The morphological evolution agrees with the polymorph transition observed by GIWAXS, where the filamentary crystallites can be associated to the formation of the LC phase.

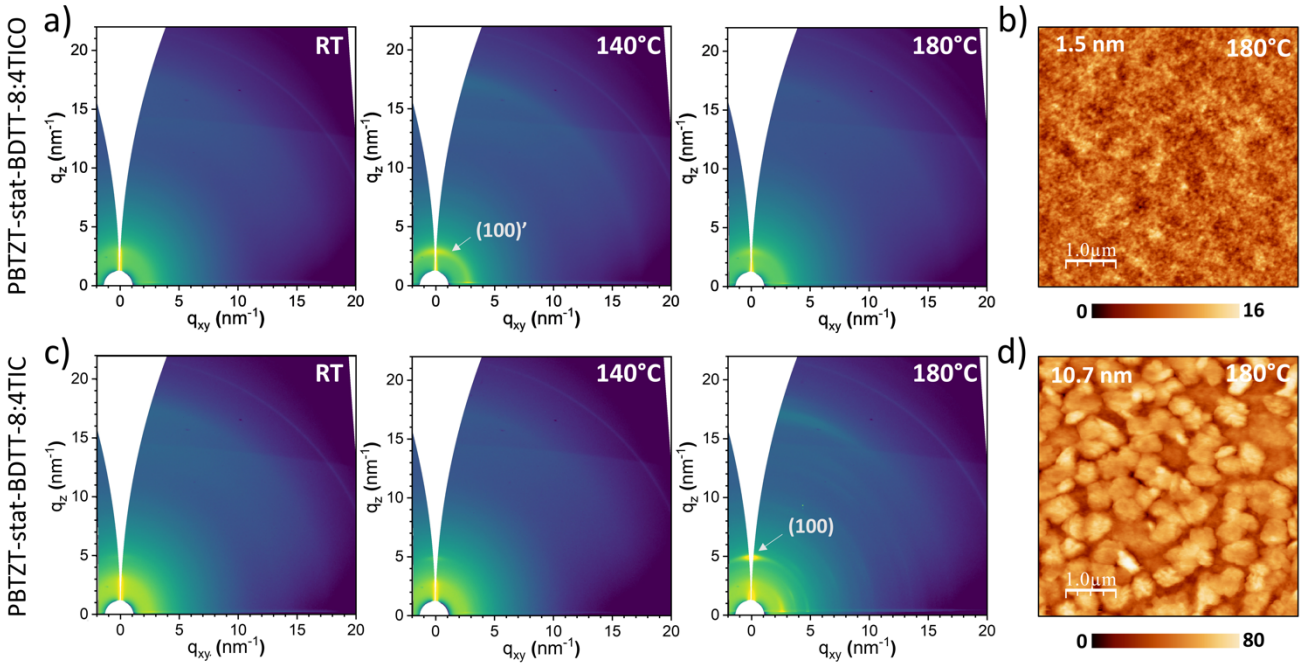

Figure 5 Structural and morphological evolution of the films of 4TICO and 4TIC blended with PBTZT-stat-BDTT-8 upon annealing treatment. 4TICO blend (a) 2D GIWAXS maps at RT and after annealing at 140°C and at 180°C and (b) 5x5 μm^2 AFM topography image and RMS after annealing at 180°C. 4TIC blend (c) 2D GIWAXS maps at RT and after annealing at 140°C and at 180°C and (d) 5x5 μm^2 AFM topography image and RMS after annealing at 180°C.

AFM analysis of 4TIC reveals no significant morphological changes up to around 120°C whereas annealing at T>140°C leads to the appearance of well-defined grains, in line with the enhanced crystallization of 4TIC, evident from GIWAXS analysis. In this case, roughness gradually increases with the annealing temperature (Figure S4).

Bulk heterojunction microstructure and morphology

The same detailed structural/morphological investigation is carried out for the pure donor PBTZT-stat-BDTT-8 and for the two donor:NFA blends. The GIWAXS study of the donor film reveals the lamellar (100) peak at q ≈ 2.7 nm^{-1}, appearing along both the OOP and IP directions. The structure remains substantially unchanged up to 140°C (Figure S5 and Table S2), as further confirmed by Uv-Vis (Figure S6) and AFM surface morphology and RMS (Figure S7-S8). Upon annealing at 180°C, we observe a clear development of π-π stacking along the OOP direction (peak at q ≈ 17.3 nm^{-1}) and a simultaneous increase of the (100) intensity along the IP direction, both indicating a dominant face-on configuration.

In the blend films, the crystalline ordering of the NFAs is not as pronounced as for the pure films. Figure 6 summarizes the GIWAXS and AFM results for the blends, highlighting the main structural changes occurring with annealing. The complete sets of GIWAXS maps and AFM images are reported in the Supporting Information.

For the PBTZT-stat-BDTT-8:4TICO blend, the absence of X-Ray scattering features in the 2D GIWAXS map at RT suggests a lack of crystalline ordering of both, donor and acceptor. After annealing at 140°C, two ring-like scattering features are clearly visible at q ≈ 2.9 nm^{-1} and q ≈ 17.4 nm^{-1}, the latest with fainter intensity (see Figure 5a, Figure S9 and Table S4). As the lamellar and short distances of PBTZT-stat-BDTT-8 and 4TICO LC phase are very similar (Table S1 and S3), the structural features of each

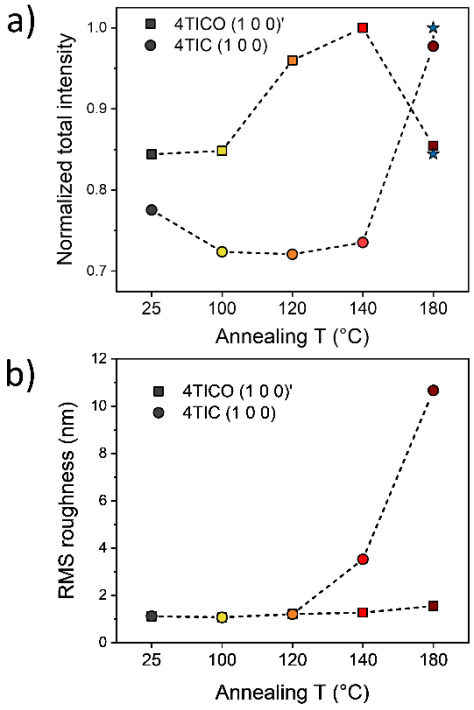

Figure 6. Main structural and morphological traits representative of the different evolution of the two blends upon annealing treatment. (a) Total diffraction intensity evolution of the 4TICO (100)' and the 4TIC (100); the stars correspond to the cooled-down state. (b) RMS roughness evolution of the two blends.

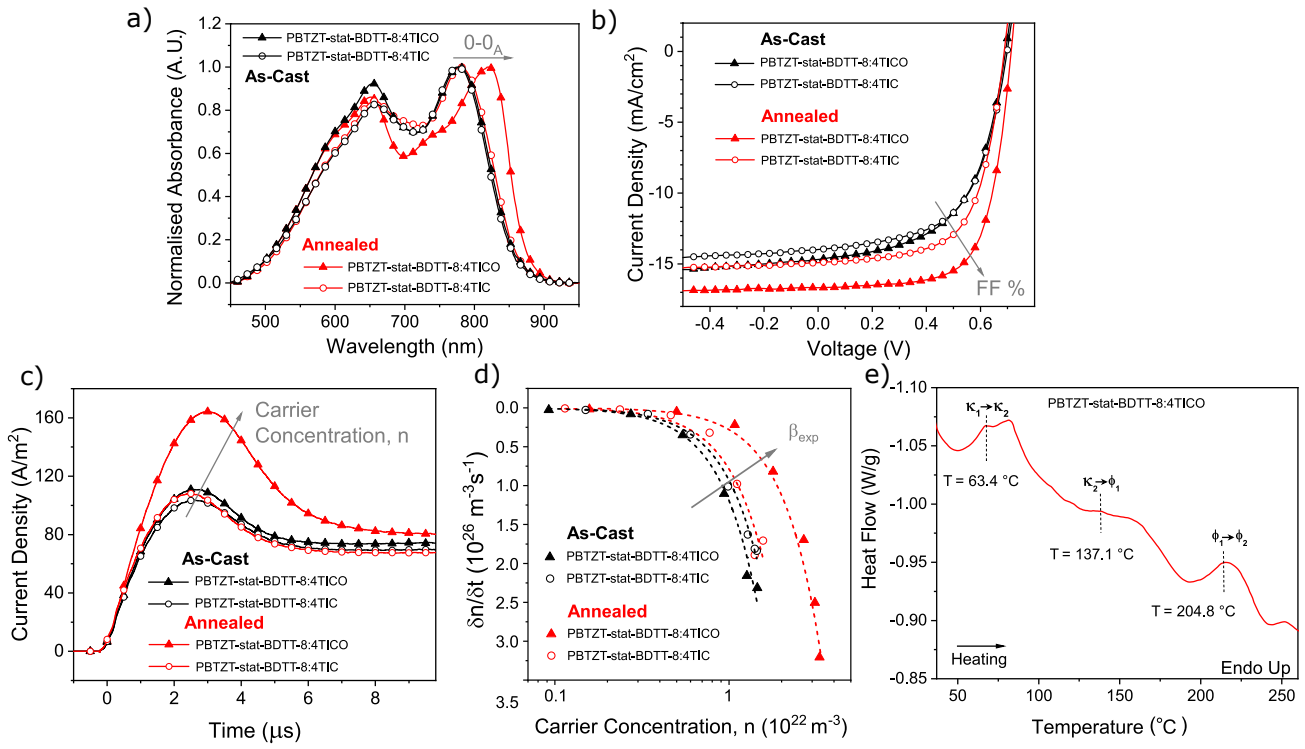

Figure 7. PBTZT-stat-BDTT-8:4TIC and PBTZT-stat-BDTT-8:4TICO active layers properties before and after annealing: UV-Vis absorptions (a) and JV characteristics (b). Charge carrier concentration (c) and recombination coefficients (d) determined by photo-CELIV. Dashed lines in (d) represent quadratic curve fits for bimolecular recombination. The effect of thermal annealing on the different measurements results is highlighted by grey arrows. e) DSC curve of PBTZT-stat-BDTT-8:4TICO blend.

material cannot be fully disentangled. Nevertheless, as the UV-Vis absorption features (red-shift) and the DSC thermogram of the PBTZT-stat-BDTT-8:4TICO blend have shown very similar trends compared to the pure 4TICO film (see Figure 7a,e), we believe that the observed structural features correspond to the 4TICO LC phase. Moreover, as visible from Figure S9, such structural features are already detected at 120°C, which means that the LC phase is stabilized in the blend at a lower temperature than for the pure film, which is possibly caused by the interaction with PBTZT-stat-BDTT-8,[80] as also reported by recent findings on PBDB-T:ITIC blends.[36] Concurrently, the AFM images do not show significant changes, revealing a very smooth nanomorphology (Figure 5b and S10). When 4TIC is blended with PBTZT-stat-BDTT-8, the film exhibits very low crystallinity, without evidence of 4TIC ordering (Figure 5c). Annealing at 180°C promotes the crystallization of the NFA, as for the pure film, but with a higher angular azimuthal distribution (see profiles in Figure S11). The 4TIC crystallization in the blend at high temperatures is accompanied by severe morphological changes (Figure 5a, Figure S12 and Table S5). Micrometric aggregates emerge on the surface, suggesting that considerable phase separation is occurring upon annealing at T>140°C.

Figure 6 summarizes two aspects that are representative of the dissimilar structural/morphological evolution of the two blends with annealing: the azimuthally integrated intensity of the lamellar peak and the film roughness. As clearly visible in Figure 6a, the signal and thus crystallinity of 4TICO in the blend increases up to 140°C and decreases upon further heating. In contrast, 4TIC exhibits an abrupt crystallization beyond 140°C as occurred for the pure material. It is thus evident that the alkoxy-phenyl sidechains of 4TICO suppress crystallization of the NFA upon heating and lead to a more intermixed nanomorphology in the PBTZT-stat-BDTT-8:4TICO blend, which remains stable in the explored temperature range (up to 180˚C). Such effect is also visible from the roughness evolution of the two blends, reported in Figure 6b. Whereas the roughness of PBTZT-stat-BDTT-8:4TICO blends shows only a slight change with temperature (remaining <2nm), a tenfold increase of the roughness is observed in the case of 4TIC at annealing temperatures higher than 140°C due to a dramatic phase separation process.

Blend properties and solar cells characteristics

To determine whether the different behaviour of 4TICO and 4TIC with thermal annealing has an effect on the solar cells' performance, we fabricate inverted architecture devices by doctor blading, using the two NFAs in combination with PBTZT-stat-BDTT-8 with a 1.3:1 ratio. The whole stack (with the only exception being the silver evaporated electrodes) was processed in air environment by using non-halogenated solvents, with the aim of meeting some of the essential requirements for the scalability and mass production of solution-processed solar panels. [81-83]

Solar cells were tested after each annealing step and the best performing devices were obtained after the final annealing performed at 140°C (Figure S13). Consequently, we limit the

following discussion to the comparison of the devices fabricated at RT and the optimized devices annealed at 140°C.

As revealed from our initial investigation on the pure materials' properties at room temperature, the two NFAs blended with PBTZT-stat-BDTT-8 have shown very similar absorption profiles (Figure 7a) and JV curves (Figure 7b) prior to annealing. As mentioned, thermal annealing has a stronger impact on the 4TICO-based solar cell when compared to the 4TIC-based one. The PBTZT-stat-BDTT-8:4TICO 0-0 vibronic peak associated to the acceptor molecule is redshifted by ~45 nm (Figure 7a) after annealing at 140°C. Such shift further confirms the formation of the 4TICO LC phase in the blends, in agreement with GIWAXS (Figure 5a) and DSC (Figure 7e). As expected from the results on the bare 4TIC film, thermal annealing has minimal impact on the PBTZT-stat-BDTT-8:4TIC blend (Figure 7a) both in terms of absorption profile and device performance.

Table 1 Photovoltaic parameters (average and standard deviation over a minimum of 6 devices) of 4TICO and 4TIC blended with PBTZT-stat-BDTT-8 before and after thermal annealing at 140°C. Pixel area is 16 mm^2. Device mobility and bimolecular recombination coefficient derived from photo-CELIV are also shown.

Active Layer	Processing Condition	PCE (%)	FF (%)	J_{SC} (mA/cm^2)	V_{OC} (mV)	μ ($cm^2/V \cdot s$)	β_{exp} (m^3/s)
PBTZT-stat-BDTT-8:4TICO	As-Cast	5.6 ± 0.3 (5.8)	57.0 ± 1.7 (59.4)	14.0 ± 0.7 (14.8)	695 ± 7 (710)	$(7 \pm 3.5) \cdot 10^{-5}$	$(1 \pm 0.5) \cdot 10^{-17}$
PBTZT-stat-BDTT-8:4TICO	Annealed	7.6 ± 0.3 (8.1)	68.5 ± 1.1 (70.9)	15.4 ± 0.8 (16.9)	718 ± 5 (725)	$(6 \pm 3) \cdot 10^{-5}$	$(3 \pm 1.5) \cdot 10^{-18}$
PBTZT-stat-BDTT-8:4TIC	As-Cast	5.6 ± 0.1 (5.7)	58.6 ± 0.3 (59.0)	13.8 ± 0.3 (14.1)	695 ± 3 (700)	$(6 \pm 3) \cdot 10^{-5}$	$(9 \pm 4.5) \cdot 10^{-18}$
PBTZT-stat-BDTT-8:4TIC	Annealed	6.4 ± 0.2 (6.6)	65.9 ± 1.4 (67.8)	14.2 ± 0.3 (14.7)	688 ± 6 (695)	$(7 \pm 3.5) \cdot 10^{-5}$	$(8 \pm 4) \cdot 10^{-18}$

Regarding the solar cell performance, both systems improve upon annealing but to a different extent: the PCE of the PBTZT-stat-BDTT-8:4TICO is enhanced by about 40%, while the PBTZT-stat-BDTT-8:4TIC PCE improves by about 15% (Figure 7b and Table 1).

While the J_{sc} improvements of PBTZT-stat-BDTT-8:4TICO could in part be explained by absorption spectra broadening during the annealing (Figure 7a), the FF increase suggests possible underlying change in charge transport properties (assuming similar extraction dynamics). For this reason, we have performed a comparative study of the charge carrier mobility and recombination dynamics on both as-cast and annealed (140°C) blends by charge extraction experiments (photo-CELIV) on the same devices. The obtained mobility values are listed in Table 1. The values are comparable to those reported for other donor:NFA blends studied with a similar approach.[65] As mobility values are comparable for the two blends (both as-cast and annealed), a more in-depth analysis on charge recombination has been carried out. Non-geminate recombination is recognised to be one of the main loss mechanisms in organic solar cells.[84] As carriers of opposite charges are photogenerated pairwise, the bimolecular recombination rate can be derived experimentally using the following expression:[64]

$$\frac{dn}{dt} = -\beta_{exp} \cdot n^2$$

where n is the charge carrier density and β_{exp} the experimentally derived bimolecular recombination coefficient.

As shown in Figure 7d and Table 1, the bimolecular recombination coefficient (β_{exp}) is significantly reduced for the PBTZT-stat-BDTT-8:4TICO blend. This may lead to the increase of the extracted photogenerated charges, which contributes to the higher FF and J_{SC} of the PBTZT-stat-BDTT-8:4TICO blend after annealing. Moreover, a slight rise in V_{oc} is also observed after annealing as a result of the reduced bimolecular recombination.[85] We attribute the significant reduction of β_{exp} to the formation of a liquid crystalline phase upon annealing. Liquid crystals can improve the grain interconnectivity and act as a healing factor with respect to structural impurities at the interfaces,[86] which are responsible for charge accumulation and recombination centres.[22] Moreover, the liquid crystal nature of 4TICO offers a larger temperature window for devices optimisation since it allows a intermixed morphology after thermal annealing at 140 °C.

Discussion (in context with literature)

In other reports focused on indacenodithienothiophene-based NFAs, the formation of a high-temperature polymorph was shown to be detrimental for the device performance as a consequence of a reduced optical absorption [60] and excessive phase separation,[36] while a similar study has proven how annealing-induced polymorphism can aid to the formation of a more functional interface between donor and acceptor,[87] leading to higher J_{sc} and FF. In our experiments, we have observed how the formation of a liquid crystalline phase can be beneficial to the solar cells' performance. As illustrated in previous studies, the use of liquid crystalline compounds can improve the charge transport properties in solar cells.[54, 55, 86] In particular, the incorporation of liquid crystalline compounds in the active layer, such as BTR and TP derivatives, has led to improvements in charge transport properties, characterised by higher fill factors[54, 88] and reduced bimolecular recombination.[51, 55, 89] It has also been observed how the self-organisation properties of liquid crystals tend to reduce

structural and electronic defects, which may act as recombination sites, thanks to their self-healing capability. This allowed to control the active layer morphology to increase the performance.[50, 89, 90]

Our results show the formation of an intermixed donor:acceptor nanomorphology, with the suppression of a detrimental (micrometre-size) NFA crystallization and drastic reduction of the bimolecular recombination upon thermal annealing, when a NFA with liquid crystalline properties is used. We believe that NFAs, being aromatic small molecules with many sidechains, have opportunities to draw design cues from the large design space that liquid crystal research has developed over the past 40 years.

We therefore encourage the OPV community to explore different routes in the chemical design to impart liquid crystalline properties in OPV materials. This can generally be obtained with different approaches: 1) by introducing additional sidechains on the molecular backbones,[51, 54, 55] (2) increasing the side-chain flexibility by introducing oxygen atoms as in 4TICO (*e.g.* alkoxy and ethylene glycol groups),[86, 91, 92] which promotes an efficient space-filling of the free volume around the molecular backbone, or (3) by targeting molecular chirality to induce a supramolecular periodicity.[93]

Conclusions

We have here presented the thermotropic behaviour of a novel NFA, 4TICO, in comparison with the related 4TIC. The peculiarity of the 4TICO versus the 4TIC is the replacement of the common phenyl-alkyl sidechains with a phenyl-alkoxy counterpart, which confers more structural flexibility due to the higher degree of freedom offered by the additional sp^2 hybridisation of oxygen atoms. As a result, the 4TICO flexibility allows a structural polymorphism which can be used as a handle to fine tune the BHJ morphology resulting in an improved microstructure and performance. In particular, the formation of a liquid crystal phase at high temperature favours the formation of a smooth surface morphology with reduced structural defects. As a consequence, non-geminate recombination was reduced by a factor of 4 when the LC phase and new morphology are formed, and the PCE is consequently increased by 40% from room temperature to 140 °C annealed solar cells.

The presented work demonstrates how important the thermotropic characteristics of NFA-based materials and films can be to optimizing device performance. Based on these results we would encourage more researchers to systematically characterize the thermotropic behaviour of newly developed OPV materials in order to better optimize their performance in the BHJ. We also hope that material chemists can also use the design cue of adding more structural flexibility to the sidechains of NFAs to enable the integration of complex liquid crystalline behaviour in these classes of compounds.

Conflicts of interest

There are no conflicts to declare.

Acknowledgements

P. M. and F. S. acknowledge the European Union's Horizon 2020 research and innovation programme under Marie Skłodowska Curie Grant agreement no. 722651 (SEPOMO) for the support in the realization of this work.

This work has been supported by the Spanish Government under the project PID2019-110907GB-I00, the "Severo Ochoa" Program for Centres of Excellence in R&D (CEX2019-000917-S) and by the European Union's Horizon 2020 Research and Innovation Program under grant agreement no. 730872. E.B. and F.S. also acknowledge the Generalitat de Catalunya grant 2017 SGR668. P.M has carried out his work within the framework of the doctoral program (PhD) in Optics and Photonics of Condensed Matter Physics (Department of Physics) at the Chemnitz University of Technology and F. S. in Material Science (Department of Physics) at the Universitat Autònoma de Barcelona (UAB). GIWAXS experiments were performed at NCD-SWEET beamline at ALBA synchrotron (Beamtime ID: 2019093873) with the collaboration of ALBA staff.

The authors thank Dr Pascal Kaienburg of the University of Oxford and Dr Mariano Campoy-Quiles of ICMAB for their valuable suggestions and fruitful discussions.

References

1. L. Xie, W. Song, J. Ge, B. Tang, X. Zhang, T. Wu and Z. Ge, *Nano Energy*, 2021, 105770.
2. P. Meredith, W. Li and A. Armin, *Advanced Energy Materials*, 2020, **10**, 2001788.
3. Y. J. Qishi Liu, Ke Jin, Jianqiang Qin, Jingui Xu, Wenting Li, Ji Xiong, Jinfeng Liu, Zuo Xiao, Kuan Sun, Shangfeng Yang, Xiaotao Zhang, Liming Ding, *Science Bulletin*, 2020.
4. P. Cheng and Y. Yang, *Accounts of chemical research*, 2020, **53**, 1218-1228.
5. J. Benduhn, K. Tvingstedt, F. Piersimoni, S. Ullbrich, Y. Fan, M. Tropiano, K. A. McGarry, O. Zeika, M. K. Riede, C. J. Douglas, S. Barlow, S. R. Marder, D. Neher, D. Spoltore and K. Vandewal, *Nature Energy*, 2017, **2**, 17053.
6. U. Wurfel, D. Neher, A. Spies and S. Albrecht, *Nat Commun*, 2015, **6**, 6951.
7. D. Qian, B. Liu, S. Wang, S. Himmelberger, M. Linares, M. Vagin, C. Müller, Z. Ma, S. Fabiano and M. Berggren, *Journal of Materials Chemistry A*, 2015, **3**, 24349-24357.
8. W. Zhu, A. P. Spencer, S. Mukherjee, J. M. Alzola, V. K. Sangwan, S. H. Amsterdam, S. M. Swick, L. O. Jones, M. C. Heiber and A. A. Herzing, *Journal of the American Chemical Society*, 2020, **142**, 14532-14547.
9. Y. Z. Huan Li, Jin Fang, Xiangwei Zhu, Benzheng, K. L. Xia, * Zhen Wang, Jianqi Zhang, Xuefeng Guo, and and Z. Wei*, *Advanced Energy Materials*, 2018, **8**.
10. F. Liu, Y. Gu, J. W. Jung, W. H. Jo and T. P. Russell, *Journal of Polymer Science Part B: Polymer Physics*, 2012, **50**, 1018-1044.
11. P. Müller-Buschbaum, *Advanced materials*, 2014, **26**, 7692-7709.

12. R. Mauer, I. A. Howard and F. Laquai, *The Journal of Physical Chemistry Letters*, 2010, **1**, 3500-3505.
13. R. S. Gurney, D. G. Lidzey and T. Wang, *Reports on Progress in Physics*, 2019, **82**, 036601.
14. L. Yang, Z. Hu, Z. Zhang, J. Cao, H. Wang, J. Yu, F. Zhang and W. Tang, *Journal of Materials Chemistry A*, 2020, **8**, 5458-5466.
15. S. M. Swick, W. Zhu, M. Matta, T. J. Aldrich, A. Harbuzaru, J. T. Lopez Navarrete, R. Ponce Ortiz, K. L. Kohlstedt, G. C. Schatz, A. Facchetti, F. S. Melkonyan and T. J. Marks, *Proc Natl Acad Sci U S A*, 2018, DOI: 10.1073/pnas.1807535115.
16. X. Li, H. Huang, I. Angunawela, J. Zhou, J. Du, A. Liebman-Pelaez, C. Zhu, Z. Zhang, L. Meng and Z. Xie, *Advanced Functional Materials*, 2020, **30**, 1906855.
17. D. Mo, H. Chen, J. Zhou, N. Tang, L. Han, Y. Zhu, P. Chao, H. Lai, Z. Xie and F. He, *Journal of Materials Chemistry A*, 2020, **8**, 8903-8912.
18. S. Li, L. Ye, W. Zhao, S. Zhang, H. Ade and J. Hou, *Advanced Energy Materials*, 2017, **7**, 1700183.
19. Y. Zhang, Z. Liu, T. Shan, Y. Wang, L. Zhu, T. Li, F. Liu and H. Zhong, *Materials Chemistry Frontiers*, 2020.
20. R. Yu, H. Yao, L. Hong, Y. Qin, J. Zhu, Y. Cui, S. Li and J. Hou, *Nature Communications*, 2018, **9**.
21. J. T. Rogers, K. Schmidt, M. F. Toney, E. J. Kramer and G. C. Bazan, *Advanced materials*, 2011, **23**, 2284-2288.
22. S. Mukherjee, C. M. Proctor, J. R. Tumbleston, G. C. Bazan, T. Q. Nguyen and H. Ade, *Advanced Materials*, 2015, **27**, 1105-1111.
23. M. Shao, J. K. Keum, R. Kumar, J. Chen, J. F. Browning, S. Das, W. Chen, J. Hou, C. Do and K. C. Littrell, *Advanced Functional Materials*, 2014, **24**, 6647-6657.
24. C. McDowell, M. Abdelsamie, M. F. Toney and G. C. Bazan, *Advanced Materials*, 2018, **30**, 1707114.
25. J. Liu, J. Han, Q. Liang, J. Xin, Y. Tang, W. Ma, X. Yu and Y. Han, *ACS omega*, 2018, **3**, 7603-7612.
26. Y. Qin, Y. Xu, Z. Peng, J. Hou and H. Ade, *Advanced Functional Materials*, 2020, **30**, 2005011.
27. Y. Liu, J. Zhao, Z. Li, C. Mu, W. Ma, H. Hu, K. Jiang, H. Lin, H. Ade and H. Yan, *Nat Commun*, 2014, **5**, 5293.
28. F. Padinger, R. S. Rittberger and N. S. Sariciftci, *Advanced Functional Materials*, 2003, **13**, 85-88.
29. T. J. Savenije, J. E. Kroeze, X. Yang and J. Loos, *Advanced Functional Materials*, 2005, **15**, 1260-1266.
30. M. Campoy-Quiles, T. Ferenczi, T. Agostinelli, P. G. Etchegoin, Y. Kim, T. D. Anthopoulos, P. N. Stavrinou, D. D. Bradley and J. Nelson, *Nat Mater*, 2008, **7**, 158-164.
31. H.-H. Gao, Y. Sun, X. Wan, B. Kan, X. Ke, H. Zhang, C. Li and Y. Chen, *Science China Materials*, 2017, **60**, 819-828.
32. C. B. Meier, R. S. Sprick, A. Monti, P. Guiglion, J.-S. M. Lee, M. A. Zwijnenburg and A. I. Cooper, *Polymer*, 2017, **126**, 283-290.
33. L. Zhang, B. Lin, Z. Ke, J. Chen, W. Li, M. Zhang and W. Ma, *Nano Energy*, 2017, **41**, 609-617.
34. T. Agostinelli, S. Lilliu, J. G. Labram, M. Campoy-Quiles, M. Hampton, E. Pires, J. Rawle, O. Bikondoa, D. D. Bradley and T. D. Anthopoulos, *Advanced Functional Materials*, 2011, **21**, 1701-1708.
35. Q. Liang, J. Han, C. Song, X. Yu, D.-M. Smilgies, K. Zhao, J. Liu and Y. Han, *Journal of Materials Chemistry A*, 2018, **6**, 15610-15620.
36. L. Yu, D. Qian, S. Marina, F. A. Nugroho, A. Sharma, S. Hultmark, A. I. Hofmann, R. Kroon, J. Benduhn and D.-M. Smilgies, *ACS applied materials & interfaces*, 2019, **11**, 21766-21774.
37. F. C. Krebs, T. Tromholt and M. Jørgensen, *Nanoscale*, 2010, **2**, 873-886.
38. W. Pisula, M. Zorn, J. Y. Chang, K. Müllen and R. Zentel, *Macromolecular rapid communications*, 2009, **30**, 1179-1202.
39. S. Laschat, A. Baro, N. Steinke, F. Giesselmann, C. Hagele, G. Scalia, R. Judele, E. Kapatsina, S. Sauer, A. Schreivogel and M. Tosoni, *Angew Chem Int Ed Engl*, 2007, **46**, 4832-4887.
40. W. W. Wong, T. B. Singh, D. Vak, W. Pisula, C. Yan, X. Feng, E. L. Williams, K. L. Chan, Q. Mao and D. J. Jones, *Advanced Functional Materials*, 2010, **20**, 927-938.
41. S. J. Kang, S. Ahn, J. B. Kim, C. Schenck, A. M. Hiszpanski, S. Oh, T. Schiros, Y.-L. Loo and C. Nuckolls, *Journal of the American Chemical Society*, 2013, **135**, 2207-2212.
42. L. Schmidt-Mende, A. Fechtenkötter, K. Müllen, E. Moons, R. H. Friend and J. D. MacKenzie, *Science*, 2001, **293**, 1119-1122.
43. J. Li, M. Kastler, W. Pisula, J. W. F. Robertson, D. Wasserfallen, A. C. Grimsdale, J. Wu and K. Müllen, *Advanced Functional Materials*, 2007, **17**, 2528-2533.
44. L. Schmidt-Mende, M. Watson, K. Müllen and R. H. Friend, *Molecular Crystals and Liquid Crystals*, 2003, **396**, 73-90.
45. L. Schmidt-Mende, A. Fechtenkötter, K. Müllen, R. H. Friend and J. MacKenzie, *Physica E: Low-dimensional Systems and Nanostructures*, 2002, **14**, 263-267.
46. T. Hori, Y. Miyake, N. Yamasaki, H. Yoshida, A. Fujii, Y. Shimizu and M. Ozaki, *Applied physics express*, 2010, **3**, 101602.
47. Q.-D. Dao, T. Saito, S. Nakano, H. Fukui, T. Kamikado, A. Fujii, Y. Shimizu and M. Ozaki, *Applied Physics Express*, 2013, **6**, 122301.
48. T. Hori, T. Masuda, N. Fukuoka, T. Hayashi, Y. Miyake, T. Kamikado, H. Yoshida, A. Fujii, Y. Shimizu and M. Ozaki, *Organic Electronics*, 2012, **13**, 335-340.
49. R. J. Bushby and O. R. Lozman, *Current Opinion in Solid State and Materials Science*, 2002, **6**, 569-578.
50. M. Bajpai, N. Yadav, S. Kumar, R. Srivastava and R. Dhar, *Liquid Crystals*, 2016, **43**, 305-313.
51. H. Li, Q. Wu, R. Zhou, Y. Shi, C. Yang, Y. Zhang, J. Zhang, W. Zou, D. Deng and K. Lu, *Advanced Energy Materials*, 2019, **9**, 1803175.
52. H. Chen, D. Hu, Q. Yang, J. Gao, J. Fu, K. Yang, H. He, S. Chen, Z. Kan and T. Duan, *Joule*, 2019, **3**, 3034-3047.
53. A. J. Bourque, S. Engmann, A. Fuster, C. R. Snyder, L. J. Richter, P. B. Geraghty and D. J. Jones, *Journal of Materials Chemistry A*, 2019, **7**, 16458-16471.
54. K. Sun, Z. Xiao, S. Lu, W. Zajaczkowski, W. Pisula, E. Hanssen, J. M. White, R. M. Williamson, J. Subbiah, J. Ouyang, A. B. Holmes, W. W. Wong and D. J. Jones, *Nat Commun*, 2015, **6**, 6013.
55. G. Zhang, K. Zhang, Q. Yin, X.-F. Jiang, Z. Wang, J. Xin, W. Ma, H. Yan, F. Huang and Y. Cao, *Journal of the American Chemical Society*, 2017, **139**, 2387-2395.
56. R. J. Bushby, I. W. Hamley, Q. Liu, O. R. Lozman and J. E. Lydon, *Journal of Materials Chemistry*, 2005, **15**, 4429-4434.
57. P. Mondelli, G. Boschetto, P. N. Horton, P. Tiwana, C.-K. Skylaris, S. J. Coles, M. Krompiec and G. Morse, *Materials Horizons*, 2020, **7**, 1062-1072.

58. X. Shi, L. Zuo, S. B. Jo, K. Gao, F. Lin, F. Liu and A. K. Y. Jen, *Chemistry of Materials*, 2017, **29**, 8369-8376.
59. E. Wang, J. Bergqvist, K. Vandewal, Z. Ma, L. Hou, A. Lundin, S. Himmelberger, A. Salleo, C. Müller and O. Inganäs, *Advanced Energy Materials*, 2013, **3**, 806-814.
60. S. Marina, A. D. Scaccabarozzi, E. Gutierrez-Fernandez, E. Solano, A. Khirbat, L. Ciammaruchi, A. Iturrospe, A. Balzer, L. Yu and E. Gabirondo, *Advanced Functional Materials*, 2021, 2103784.
61. S. Berny, N. Blouin, A. Distler, H. J. Egelhaaf, M. Krompiec, A. Lohr, O. R. Lozman, G. E. Morse, L. Nanson, A. Pron, T. Sauermann, N. Seidler, S. Tierney, P. Tiwana, M. Wagner and H. Wilson, *Adv Sci (Weinh)*, 2016, **3**, 1500342.
62. G. Ashiotis, A. Deschildre, Z. Nawaz, J. P. Wright, D. Karkoulis, F. E. Picca and J. Kieffer, *Journal of applied crystallography*, 2015, **48**, 510-519.
63. I. Horcas, R. Fernández, J. Gomez-Rodriguez, J. Colchero, J. Gómez-Herrero and A. Baro, *Review of scientific instruments*, 2007, **78**, 013705.
64. T. M. Clarke, C. Lungenschmied, J. Peet, N. Drolet and A. J. Mozer, *Advanced Energy Materials*, 2015, **5**, 1401345.
65. A. Baumann, J. Lorrmann, D. Rauh, C. Deibel and V. Dyakonov, *Advanced Materials*, 2012, **24**, 4381-4386.
66. J. Gorenflot, M. C. Heiber, A. Baumann, J. Lorrmann, M. Gunz, A. Kämpgen, V. Dyakonov and C. Deibel, *Journal of Applied Physics*, 2014, **115**, 144502.
67. D. Murthy, A. Melianas, Z. Tang, G. Juška, K. Arlauskas, F. Zhang, L. D. Siebbeles, O. Inganäs and T. J. Savenije, *Advanced Functional Materials*, 2013, **23**, 4262-4268.
68. S. Chen, K. R. Choudhury, J. Subbiah, C. M. Amb, J. R. Reynolds and F. So, *Advanced Energy Materials*, 2011, **1**, 963-969.
69. A. Baumann, T. J. Savenije, D. H. K. Murthy, M. Heeney, V. Dyakonov and C. Deibel, *Advanced Functional Materials*, 2011, **21**, 1687-1692.
70. G. Dennler, A. J. Mozer, G. Juška, A. Pivrikas, R. Österbacka, A. Fuchsbauer and N. S. Sariciftci, *Organic Electronics*, 2006, **7**, 229-234.
71. A. J. Mozer, N. S. Sariciftci, L. Lutsen, D. Vanderzande, R. Österbacka, M. Westerling and G. Juška, *Applied Physics Letters*, 2005, **86**, 112104.
72. a. Meera Stephen, b* KristijonasGenevi˘, b. G. J. cius, b Kestutis and A. a. R. C. Hiornsc*, *Polym. Int.*, 2017, **66**.
73. G. Juška, K. Arlauskas, M. Viliūnas and J. Kočka, *Physical review letters*, 2000, **84**, 4946.
74. M. T. Neukom, N. A. Reinke and B. Ruhstaller, *Solar Energy*, 2011, **85**, 1250-1256.
75. O. J. Sandberg and M. Nyman, *Organic Electronics*, 2019, **64**, 97-103.
76. P. Barois, in *Handbook of Liquid Crystals*, 1998, DOI: https://doi.org/10.1002/9783527620760.ch7f, pp. 281-405.
77. Y. Xiao and X. Lu, *Materials Today Nano*, 2019, 100030.
78. S. C. B. M. Jonathan Rivnay, Chad E. Miller, Alberto Salleo, and Michael F. Toney, *chemical Reviews*, 2012, **112**.
79. R. Zniber, R. Achour, M. Z. Cherkaoui, B. Donnio, L. Gehringer and D. Guillon, *Journal of Materials Chemistry*, 2002, **12**, 2208-2213.
80. J. Xin, X. Meng, X. Xu, Q. Zhu, H. B. Naveed and W. Ma, *Matter*, 2019, **1**, 1316-1330.
81. L. Ye, Y. Xiong, Q. Zhang, S. Li, C. Wang, Z. Jiang, J. Hou, W. You and H. Ade, *Adv Mater*, 2018, **30**.
82. H. W. Ro, J. M. Downing, S. Engmann, A. A. Herzing, D. M. DeLongchamp, L. J. Richter, S. Mukherjee, H. Ade, M. Abdelsamie and L. K. Jagadamma, *Energy & Environmental Science*, 2016, **9**, 2835-2846.
83. L. Hong, H. Yao, Z. Wu, Y. Cui, T. Zhang, Y. Xu, R. Yu, Q. Liao, B. Gao and K. Xian, *Advanced Materials*, 2019, **31**, 1903441.
84. G. Lakhwani, A. Rao and R. H. Friend, *Annual review of physical chemistry*, 2014, **65**, 557-581.
85. D. Credgington and J. R. Durrant, *The Journal of Physical Chemistry Letters*, 2012, **3**, 1465-1478.
86. M.-A. Muth, G. Gupta, A. Wicklein, M. Carrasco-Orozco, T. Thurn-Albrecht and M. Thelakkat, *The Journal of Physical Chemistry C*, 2013, **118**, 92-102.
87. W. Köntges, P. Perkhun, J. Kammerer, R. Alkarsifi, U. Würfel, O. Margeat, C. Videlot-Ackermann, J.-J. Simon, R. R. Schröder and J. Ackermann, *Energy & Environmental Science*, 2020, **13**, 1259-1268.
88. Q. Zheng, G. Fang, W. Bai, N. Sun, P. Qin, X. Fan, F. Cheng, L. Yuan and X. Zhao, *Solar energy materials and solar cells*, 2011, **95**, 2200-2205.
89. K. N. Schwarz, P. B. Geraghty, D. J. Jones, T. A. Smith and K. P. Ghiggino, *The Journal of Physical Chemistry C*, 2016, **120**, 24002-24010.
90. X. Chen, L. Chen, K. Yao and Y. Chen, *ACS applied materials & interfaces*, 2013, **5**, 8321-8328.
91. M. R. Hansen, T. Schnitzler, W. Pisula, R. Graf, K. Müllen and H. W. Spiess, *Angewandte Chemie International Edition*, 2009, **48**, 4621-4624.
92. P. Kohn, L. Ghazaryan, G. Gupta, M. Sommer, A. Wicklein, M. Thelakkat and T. Thurn-Albrecht, *Macromolecules*, 2012, **45**, 5676-5683.
93. M. Funahashi, *Symmetry*, 2021, **13**, 672.